



Interactions between nanoscale zerovalent iron (NZVI) and silver nanoparticles alter the NZVI reactivity in aqueous environments

J. Deng, S. Yoon, M. Pasturel, S. Bae, Khalil Hanna

► To cite this version:

J. Deng, S. Yoon, M. Pasturel, S. Bae, Khalil Hanna. Interactions between nanoscale zerovalent iron (NZVI) and silver nanoparticles alter the NZVI reactivity in aqueous environments. *Chemical Engineering Journal*, 2022, 450, pp.138406. <10.1016/j.cej.2022.138406>. <hal-03780242>

HAL Id: hal-03780242

<https://hal.science/hal-03780242v1>

Submitted on 9 Feb 2023

HAL is a multi-disciplinary open access archive for the deposit and dissemination of scientific research documents, whether they are published or not. The documents may come from teaching and research institutions in France or abroad, or from public or private research centers.

L'archive ouverte pluridisciplinaire **HAL**, est destinée au dépôt et à la diffusion de documents scientifiques de niveau recherche, publiés ou non, émanant des établissements d'enseignement et de recherche français ou étrangers, des laboratoires publics ou privés.



HAL Authorization

1

2

3

4

5

6

7

8

9

10

11

12

13

14

15

16

17

Interactions between nanoscale zerovalent iron (NZVI) and silver nanoparticles alter the NZVI reactivity in aqueous environments

Junmin Deng¹, Sunho Yoon², Mathieu Pasturel³, Sungjun Bae^{2*}, Khalil Hanna^{1*}

¹ *Univ. Rennes, Ecole Nationale Supérieure de Chimie de Rennes, CNRS, ISCR-UMR*

6226, F-35000 Rennes, France

² *Department of Civil and Environmental Engineering, Konkuk University, 120*

Neungdong-ro, Gwangjin-gu, Seoul 05029, Republic of Korea

³ *Univ. Rennes, CNRS, ISCR – UMR 6226, F-35000 Rennes, France*

*Co-corresponding authors: khalil.hanna@ensc-rennes.fr and bsj1003@konkuk.ac.kr

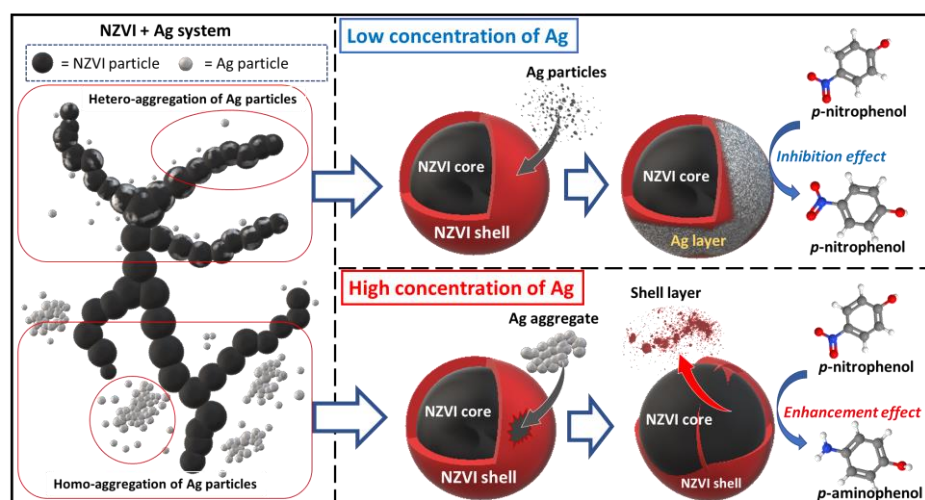
ABSTRACT

The increasing production and broad application of engineered nanoparticles (ENPs) have led to a substantial release of ENPs into natural systems. Despite their different utilization prospects, ENPs such as nanoscale zero-valent iron (NZVI) and silver nanoparticles (AgNPs) have been co-found in aquatic environments. This study comprehensively examined the effect of AgNPs on the reductive ability of NZVI, which was probed through the conversion of *p*-nitrophenol (*p*-NP) to *p*-aminophenol (*p*-AP). Electron microscopic and spectroscopic investigations and Derjaguin–Landau–Verwey–Overbeek (DLVO) calculations showed that the aggregation of NZVI with a low dose of AgNPs dramatically decreased the NZVI reactivity. In contrast, enhanced NZVI reactivity was observed when a high dose of AgNPs was used. The collision between self-assembled aggregates of AgNPs and NZVI can lead to the exposure of inner Fe(0), thereby improving the reductive ability of NZVI. The same behavior was observed for other nanosized (e.g., TiO₂) and micro-sized (e.g., quartz sand) particles, which suggests the predominance of physical processes in NZVI peeling. Further investigations showed that the presence of sulfate and humic acid enhanced the *p*-NP removal in the NZVI-AgNP suspension, in contrast to other groundwater constituents. Our findings provide a better understanding of potential ENP interactions, particularly in the context of groundwater remediation.

Keywords: nanoscale zerovalent iron; silver nanoparticles; *p*-nitrophenol; aggregation.

Graphical Abstract

Interactions between nanoscale zero-valent iron (NZVI) and silver nanoparticles (AgNPs) significantly alter the reductive ability of NZVI



1. Introduction

Over the past decades, due to increasing production and broad applications of engineered nanoparticles (ENPs), such as textile (Lorenz et al., 2012), electronics (Poudel and Kim, 2022; Poudel et al., 2021), pharmaceuticals (Sridhar et al., 2015), environmental remediation (Poudel et al. 2022) and cosmetics (Auffan et al., 2010), a significant amount of ENPs are ended up into natural systems (Abbas et al., 2020; Danaïl and Ineke, 2009). In particular, silver nanoparticles (AgNPs) are one of the most commonly used ENPs. Their catalytic ability, high surface area to volume ratio and antibacterial activity provide them with excellent potential for various industrial (Poudel et al., 2020; Shen et al., 2014), food (Echegoyen and Nerín, 2013) and medical applications (Deng et al., 2016). However, their release and accumulation in the environment (water and soil) (McGillicuddy et al., 2018; Mahdi et al., 2017) is of concern owing to their potential adverse effects on human health and aquatic life (Asghari et al., 2012; Xu et al., 2013). In the meanwhile, nanoscale zero-valent iron (NZVI), as one of the most extensively used ENPs, has been widely applied for groundwater remediation and wastewater treatment because of its high reactivity, cost-effectiveness, and environmental friendliness (Li et al., 2017; Phenrat et al., 2016; Wei et al., 2010; Xia et al., 2017). NZVI can be used to treat various contaminants such as persistent organic pollutants (Joo et al., 2004), toxic inorganic contaminants (Ryu et al., 2011) and even radioactive nuclides (Tsarev et al., 2017).

When AgNPs are discharged into terrestrial or aquatic environments, their

interaction with other co-existing ENPs could influence their environmental behavior, fate, and likely their ecotoxicity. In addition, AgNPs can potentially alter the reactivity of other ENPs used for decontamination, such as NZVI. The injection of NZVI slurry is a common method for the *in situ* remediations of aquifer and groundwater contamination by organic or inorganic compounds (Su et al., 2013; Mueller et al., 2012). Despite the possible co-occurrence of both ENPs in aquatic environments (Stefaniuk et al., 2016; Syafiuddin et al., 2018), there is a lack of knowledge on their potential interactions. Therefore, a comprehensive study on the interactions between NZVI and AgNPs is needed considering the contaminant removal methods used in remediation processes.

Herein, we selected *p*-nitrophenol (*p*-NP), as a probe compound because the reductive conversion of *p*-NP to *p*-aminophenol (*p*-AP) is well documented, and the corresponding mass balance is easy to establish owing to the low adsorption of nitrophenol and aminophenol by metal oxides (Bae et al., 2016; Lai et al., 2014; Vilardi 2020). In order to investigate the interactions between NZVI and AgNPs and clearly highlight specific effects of AgNPs on the NZVI reductive ability, we applied a wide concentration range and high-enough dosage of AgNPs (0.5 – 100 mg/L) in NZVI suspension. Two concentrations of NZVI (25 and 50 mg/L) within the concentration range typically used in lab-experiments were investigated. The phase transformation and morphological change of NZVI and AgNPs were monitored by X-ray diffraction (XRD), X-ray photoelectron spectroscopy (XPS), and transmission electron

microscopy (TEM) with energy-dispersive X-ray spectroscopy (EDS). In addition, a theoretical investigation based on Derjaguin–Landau–Verwey–Overbeek (DLVO) calculations were conducted for the low and high doses of AgNPs. Moreover, to get more insight into the relationship between effects of ENPs and their nature, interactions of NZVI with other widely used ENPs (e.g. nanosized TiO₂ particles) and inert mineral surface (e.g. quartz sand) were also investigated. Finally, the NZVI-AgNP interactions were evaluated in the presence of naturally occurring anions and cations and natural organic matter, at levels similar to those encountered in real groundwater.

2. Materials and methods

2.1 Chemicals and materials

Sodium borohydride (NaBH₄, ≥99.0%), *p*-NP (≥99%), *p*-AP (≥98%), ferric chloride hexahydrate (FeCl₃·6H₂O, ≥99.0%), hydrochloric acid (HCl, 37%), sodium hydroxide (NaOH, ≥99.0%), sodium chloride (NaCl, ≥99.5%), sodium sulfate (Na₂SO₄, ≥99.0%), calcium chloride (CaCl₂, ≥99.9%), magnesium chloride (MgCl₂, ≥98.0%) and sodium metasilicate nonahydrate (Na₂SiO₃·9H₂O, ≥98.0%) were purchased from Sigma-Aldrich, France. Acetonitrile (99.99%, Sigma) and acetic acid (99.7%, ACROS) were used as the mobile phase for the high-performance liquid chromatography (HPLC) analysis. Leonardite humic acid (LHA) standard was purchased from the International Humic Substances Society (IHSS). Silver nano-powder (containing polyvinylpyrrolidone (PVP) as a dispersant, 99.5%, <100 nm, and PZC ~3.3) and TiO₂

nano-powder (rutile, 99.5%, 50 m²/g, <100 nm, and PZC ~5.9) were purchased from Sigma-Aldrich. Fontainebleau quartz sand (FB sand, 0.06 m²/g, 150–300 µm, PZC ~2.7) was obtained from VWR International. Based on a previously published method (Deng et al., 2020), NZVI was synthesized by reducing 0.11 M FeCl₃·6H₂O with 0.9 M NaBH₄ in an anaerobic chamber.

The glassware was soaked in 5% (v:v) HCl for at least 48 h and rinsed before use. Unless specifically stated, all solutions were prepared with deoxygenated deionized water (DDIW, 18.2 MΩ·cm), purged with nitrogen (N₂, 99.99%) for 4 h, and stored in an anaerobic chamber (JACOMEX).

2.2. Experimental and analytical methods

Batch experiments were conducted in 500 mL flask in an anaerobic chamber under dark conditions. An exact amount of NZVI (0.0125 and 0.025 g) was transferred to the flask containing 500 mL of DDIW, and the mixture was stirred at 500 rpm to prepare the samples with initial NZVI concentrations of 25 and 50 mg/L. To monitor the variations in pH and oxidation-reduction potential (ORP) throughout the experiment, we used a portable pH–ORP meter (HI991003, Hanna). After 1 h, AgNPs were introduced into the suspensions to form a mixture of NZVI and AgNPs at different Ag concentrations (0.5, 2, 10, 25, 50, and 100 mg/L). An equilibration time of 1 hour was chosen because pH and ORP values have reached constant values after 1 h of reaction time. Although this time is sufficient to obtain an equilibrated NZVI suspension under our

experimental conditions, it may not be applicable at the field-scale.

After 15 h, pH and ORP reached an equilibrium, and 2 mL of *p*-NP stock solution (25 mM) was added to the suspension to initiate the reaction with *p*-NP (0.1 mM). Subsequently, 1 mL samples were withdrawn from the suspension and then filtered through a 0.2 µm filter (Whatman) for HPLC analysis. The aqueous concentrations of *p*-NP and *p*-AP were determined using HPLC (Waters 600 controller) with a photodiode array detector (Waters 996) and a reversed-phase C18 column (250 mm × 4.6 mm i.d., 5 µm). A mobile phase (acetonitrile: water at 50:50 (v:v)) containing 0.1% formic acid was prepared and used at a flow rate of 1 mL/min in isocratic mode. In addition, mass balance of *p*-NP and *p*-AP after reaction was checked and presented in Table S1.

The same procedure was used to investigate the effects of TiO₂ nanoparticles, FB sand, and groundwater solutes on the reactivity of NZVI and NZVI/AgNPs. The AgNP dissolution experiments were conducted at pH 9 in absence of NZVI, which is similar to the working pH in presence of NZVI, at AgNP dosage of 0.5, 2, 10, 25, 50, and 100 mg/L. Although the dosage of AgNPs seems to be higher than the frequently detected concentration in natural systems, we have assessed the interactions of NZVI with AgNPs over a wide range of Fe/Ag ratios (0.5 - 50) to cover some environmentally-relevant scenarios.

After 3 d, the samples were filtered through a 0.2 µm filter to measure the amount of Ag⁺ ions by inductively coupled plasma mass spectrometry (ICP-MS, Agilent 7700x). All experiments were performed in triplicates. The data reported here are the average

of three replicated experiments, and the error bars represent the relative standard deviation.

2.3. Characterization

XRD (D8, BRUKER) was used to identify the resulting products of NZVI after reaction with *p*-NP. The resulting suspensions were first collected and washed with DDIW three times, and dried in a vacuum freeze drier (−52 °C, 24 h). The dried samples were then transferred to sample holders and treated with 1:1 (v:v) glycerol solution to avoid surface oxidation during the XRD analysis (Bae and Lee, 2014). XPS (Sigma Probe system, Thermo) analysis was performed for NZVI, AgNPs, and NZVI-AgNP samples. The power source (Al K α X-ray, 1486.7 eV) was 75 W, and the C 1s peak at 285 eV was used as a reference for the correction of surface charging effects. The morphological characterization of the NZVI and NZVI-AgNP mixtures was performed by TEM–EDS, (JEM-2100, JEOL). The average particle size of the NZVI-AgNP suspension with groundwater solutes and the zeta potential of individual particles (i.e., NZVI and AgNPs) were measured using a Zetasizer (Matec Applied Sciences). The average hydrodynamic diameter of AgNPs and NZVI were determined using time-resolved dynamic light scattering (DLS, ALV-5000, Langen).

3. Results and discussion

3.1 Effect of AgNPs on the NZVI reactivity

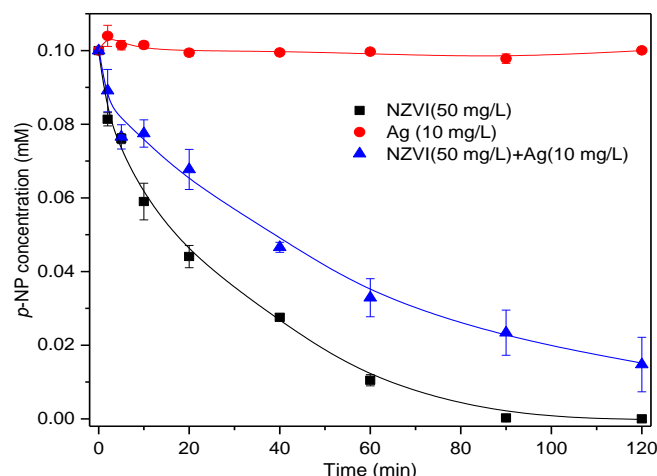


Figure 1. Concentrations of *p*-NP during the removal of *p*-NP by different nanoparticles. Experimental conditions: [*p*-NP]_{initial} = 0.1 mM; [NZVI] = 50 mg/L; [AgNPs] = 10 mg/L; pH = 9.0±0.2.

The interactions between AgNPs and NZVI were investigated under anoxic conditions by monitoring the variations in pH and ORP throughout the experiment, including at i) the addition of NZVI to the reactor, ii) addition of AgNPs, and iii) removal of *p*-NP (see Supporting Information (SI), Fig. S1). When NZVI was added to water at 50 mg/L (i.e., first 1 h), there was a clear increase in pH from 6.78 to 9.38 and a decrease in ORP from −54 to −843 mV, which were attributed to the reaction between NZVI and water (Bae and Hanna, 2015). After the addition of AgNPs at 10 mg/L to the NZVI suspension, the pH and ORP values remained constant, and only slight changes were observed in the pH and ORP after 15 h of reaction. The slight decreasing in pH and increasing in ORP value may be attributed to the consumption of Fe²⁺ and OH[−] by

the hydrolysis of ferrous under alkaline conditions (Deng et al., 2020). Afterward, little variations in pH or ORP were observed during the *p*-NP removal. Only a slight decrease in pH and increase in ORP was observed upon the addition of the *p*-NP solution.

The removal of *p*-NP by various materials, including NZVI alone, AgNPs alone, and NZVI/AgNPs mixture, was also evaluated (Fig. 1). Since the standard potential of Ag^0/Ag^+ and *p*-NP/*p*-AP is 0.79 V and 0.76 V respectively, the conversion of *p*-NP to *p*-AP by AgNPs is not likely to take place spontaneously (Hernández-Gordillo et al. 2014). Indeed, no *p*-NP removal was observed in the AgNP suspension, which indicated negligible adsorption and/or reduction of *p*-NP by AgNPs. In contrast, the complete removal of *p*-NP was observed after 90 min of reaction with NZVI, whereas 85% of *p*-NP was removed by the NZVI-AgNP suspension over 120 min. The mass balance was evaluated, which confirmed the reductive conversion of *p*-NP to *p*-AP (not shown) and the negligible adsorption of *p*-NP and *p*-AP on the NZVI surface. It is reported that the hydrogen production caused by anaerobic corrosion of NZVI could potentially affect the reduction of target contaminants (Liu and Lowry, 2006). However, the working pH was 9 in our experiments, which significantly decrease the generation of hydrogen gas (Liu and Lowry 2006). In addition, it has been generally accepted that the active H atom seems to be readily captured by reactive catalysts (e.g., Ni) rather than Fe phase, and reduction of *p*-NP could not be occurred by dissolved hydrogen alone (Du et al. 2004). Therefore, hydrogen contribution should be of minor importance in our reaction systems.

The effect of varying AgNP concentrations (0.5–100 mg/L) on the *p*-NP removal by NZVI (25 and 50 mg/L) was then investigated (Fig. S2). Nearly 72% of *p*-NP was removed by 25 mg/L of NZVI after 8 h, whereas the addition of 0.5 mg/L of AgNPs to the NZVI suspension decreased the removal to 62%. An increase in the AgNP concentration resulted in a gradual increase in the conversion of *p*-NP to *p*-AP (i.e., 64% at 2 mg/L, 84% at 10 mg/L, 89% at 25 mg/L, and 93% at 50 mg/L) (Fig. S2(a)). Similarly, the removal efficiency of *p*-NP after 2 h of reaction significantly decreased when 0.5 mg/L of AgNPs was added to a 50 mg/L NZVI suspension, and it continuously increased as the AgNP content increased (Fig. S2(b)).

To further demonstrate the variations in removal rate, we plotted the removal kinetics fitted using the pseudo-first-order equation over the early reaction stage (60 min) and the removal rate constants (k_{obs}) against AgNP dose (Fig. 2 and Fig. S2(c) and (d)). Compared to NZVI alone (0.0085 min⁻¹ at 25 mg/L, and 0.037 min⁻¹ at 50 mg/L), the obtained rate constant was nearly 1.5 and 5.8 times lower after the addition of 0.5 mg/L AgNPs. However, the k_{obs} values gradually increased to 0.0131 and 0.042 min⁻¹ as the AgNP dose increased, at 25 and 50 mg/L NZVI, respectively. Therefore, the results showed that the presence of AgNPs at a low dose significantly inhibited the NZVI reactivity, but this inhibitive effect gradually disappeared as the AgNP concentration increased.

To verify whether this two-step phenomenon was specific to AgNPs, additional investigations were conducted with nanosized TiO₂ particles (used as active

nanoparticles) and micro-sized quartz sand particles (used as an inert surface) under dark conditions. For TiO_2 , the inhibition of p -NP removal was observed at a low dosage (5 mg/L), whereas an increase in TiO_2 dose enhanced the p -NP reduction (Fig. S3). It is worth noting that TiO_2 alone showed negligible removal of p -NP at pH 9 (See Fig. S4), suggesting that possible adsorption of p -NP on TiO_2 can be excluded under our experimental conditions. However, the addition of quartz sand showed a one-step behavior, that is, the removal rate constant continuously increased with increasing sand dose (Fig. S5). Collectively, these results suggest that the increase or decrease in p -NP removal rate was not limited to the effect of AgNPs, and it likely resulted from a combination of physical and chemical processes.

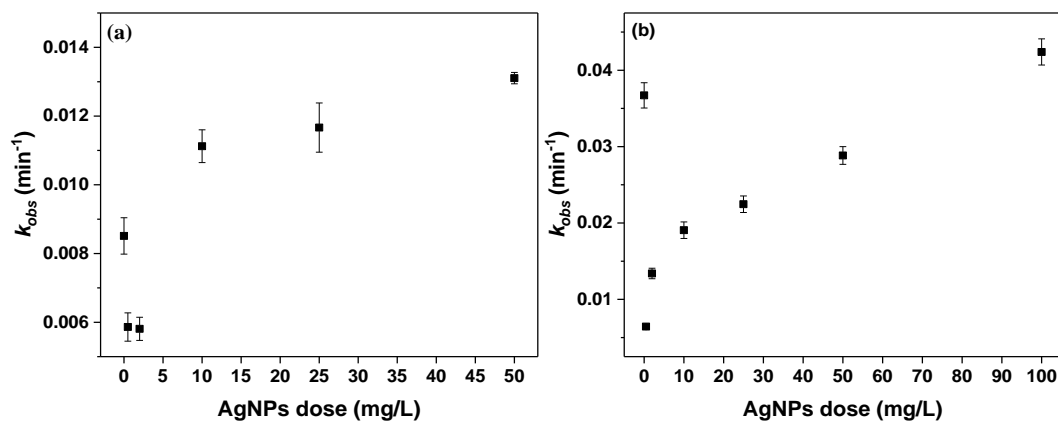


Figure 2. Variation in pseudo-first-order kinetic rate constants (k_{obs} , min^{-1}) of the removal of p -NP by NZVI with respect to AgNP dosage at (a) 25 mg/L NZVI and (b) 50 mg/L NZVI. Experimental conditions: $[p\text{-NP}]_{\text{initial}} = 0.1 \text{ mM}$; $\text{pH} = 9.0 \pm 0.2$.

3.2 Heteroaggregation and homoaggregation of AgNPs

The kinetic experiments suggested that the NZVI reactivity can be altered by the interactions between AgNPs and NZVI, which might be caused by potential aggregation and/or redox reactions between the two particles. As previously observed for goethite and hematite (Wang et al., 2019), AgNPs might bind to the surface of the oxides layer in the core-shell structure of NZVI. Accordingly, the electrostatic attraction between negatively charged AgNPs (PZC \sim 3.3) and iron oxides has been used to explain the heteroaggregation process and inhibition of AgNP dissolution (Wang et al., 2019). However, these interactions have been investigated at circumneutral pH values (5.5 and 7.5), at which the surface charge of goethite (PZC \sim 9) and hematite (PZC \sim 8) are predominately positive. This emphasizes the role of electrostatic attraction for the adsorption of negatively charged AgNPs onto iron oxides. The zeta potential of NZVI and AgNPs at different pHs were measured to gain more insight into electrostatic interactions between the two types of particle (Fig. S6). However, the working pH of the NZVI suspension lay at 9, at which the surface charge of both NPs are negative. Indeed, at pH above the PZC of minerals, dissociation of surface functional groups in water will give a negatively charged surface (Lützenkirchen et al. 2008).

To investigate the interparticle interactions in NZVI-AgNP suspensions under the experimental conditions of the present work, TEM-EDS analyses were conducted. The silver nanoparticles sample used in this study is mostly round shape with particle size in water lower than 100 nm. The NZVI showed chain-like aggregates consisting of spherical particles (60–100 nm) (Fig. 3(a)), which are generally attributed to the high

surface energy and intrinsic magnetic interaction among NZVI particles (Sohn et al., 2006). Significantly smaller particles were attached to larger particles (80–100 nm) when 10 mg/L of AgNPs was added (Fig. 3(b)). However, the attachment of small particles was not observed at a high AgNP dose (100 mg/L) (Fig. 3(c)). Instead, we observed the co-existence of chain-like aggregates and nanoparticle assemblages. The EDS mapping of NZVI-AgNP mixtures showed distinct Fe and Ag nanoparticles highlighted in red and green, respectively, in Figs. 3(d) and (e). As illustrated in Fig. 3(d), the Ag-phase was enriched near the surface of Fe aggregates at low AgNP concentrations, which suggests the heteroaggregation of NZVI and AgNPs. The spatial correlation of Ag and Fe was not observed at high AgNP concentrations (Fig. 3(e)), but these two elements existed in different locations because AgNPs tended to homoaggregate rather than interact with NZVI at higher AgNP doses. It was previously reported that aggregation behavior of NPs would change along with their oxidation (Vilardi 2019, Vilardi et al. 2019). However, similar TEM images of AgNPs and NZVI were observed after the reaction with *p*-NP (Fig. S7), suggesting no significant modification of the interactions between NZVI and AgNPs.

The enlarged TEM images with EDS mapping revealed a clear difference for different AgNP dosages (Fig. S8). In the absence of AgNPs (Fig. S8(a)), the TEM images of NZVI showed a typical shape of NZVI particles covered by a thin Fe oxide shell. The corresponding elemental mapping (Fe and O) further displayed the core-shell structure of NZVI, showing a strong signal intensity of Fe in the core, whereas O was

mostly present in the shell layer (2.5–3.5 nm). However, the thickness of the NZVI
oxide shell seems to decrease significantly after the addition of 100 mg/L AgNPs,
whereas almost no change was observed with the addition of 10 mg/L AgNPs. Based
on the TEM–EDS results, we hypothesized that AgNPs at a low dose attach to the NZVI
surfaces (i.e., iron oxides), and at a high dose, they tend to homoaggregate. We also
hypothesized that introducing a high dosage of AgNP would lead to a decrease in the
thickness of the NZVI oxide layer, which should be further investigated.

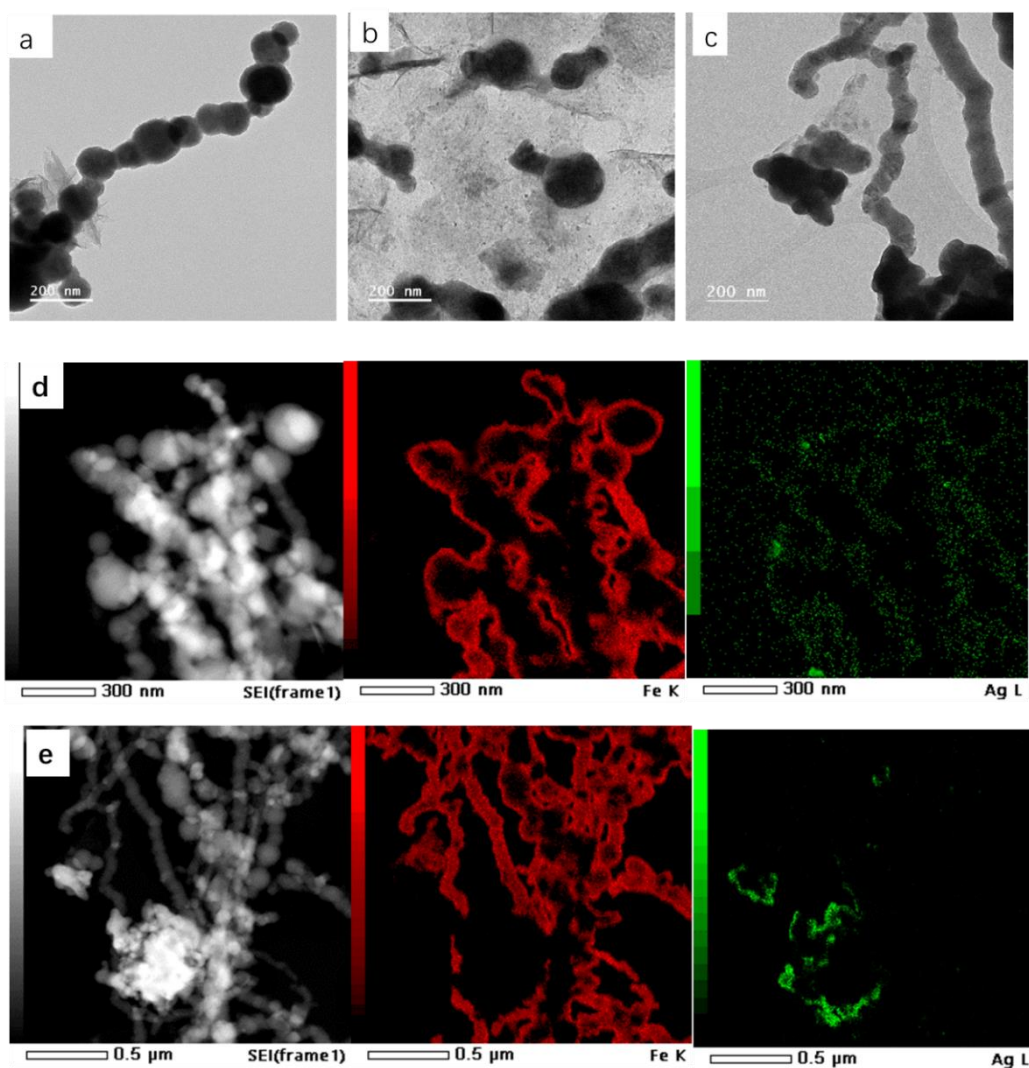


Figure 3. TEM images of (a) NZVI, (b) AgNP–NZVI at 10 mg/L AgNPs, and (c)

AgNP–NZVI at 100 mg/L AgNPs. Elemental mapping of AgNP–NZVI at AgNP doses of (d) 10 mg/L and (e) 100 mg/L. Conditions: [NZVI] = 50 mg/L.

We also analyzed the attraction and repulsion behaviors of AgNPs and NZVI according to the DLVO theory. This theory considers attractive van der Waals (vdW) and repulsive electrostatic double-layer (EDL) forces between the particles ($\Phi_{DLVO} = \Phi_{EDL} + \Phi_{vdW}$). The details of DLVO calculations are provided in the SI. In brief, at a low AgNP dose (10 mg/L), heteroaggregation (AgNP–NZVI) is likely to occur because of the lower repulsive energy barriers of AgNP–NZVI with respect to AgNP–AgNP. In addition, the AgNPs used in this study also contained stabilized PVP, so the surface coatings could serve as a bridge between coated AgNPs and uncoated NZVI to overcome the energy barrier (Lin et al., 2012). Therefore, it is likely that PVP-stabilized AgNPs formed heteroaggregates with NZVI. In contrast, a higher AgNP dose (100 mg/L) led to a significantly higher magnitude of calculated maximum repulsive interaction energies (Φ_{max}), which would not be sufficient to overcome non-DLVO energy. According to the calculations, neither heteroaggregation nor homoaggregation (AgNP–AgNP) would occur spontaneously. However, AgNP homoaggregation was still observed using TEM–EDS. This discrepancy between DLVO calculations and TEM images might be attributed to the potential chemical interactions between AgNPs and NZVI or oxide layer coating NZVI.

A recent study reported that AgNP morphology may change from a dispersed

spherical shape to larger aggregates owing to the release of Ag^+ possibly because of (i) the nano bridges created by adsorption and/or redox conversion of Ag^+ into Ag^0 at the particle surface to connect nearby particles, and (ii) the growth of reformed small AgNPs around old AgNPs (Yu et al., 2014). Other reports showed that Ag^+ released from AgNPs and possible electron transfer from Fe^0 to Ag^+ could form a galvanic couple, which may accelerate NZVI-water corrosion (Zhuang et al., 2011; Zhu et al., 2021). Therefore, interactions of Ag^+ ions ($E_0 \text{ Ag}/\text{Ag}^+ 0.799 \text{ V}$) with NZVI ($E_0 \text{ Fe}/\text{Fe}^{2+} 0.44 \text{ V}$) and AgNPs through adsorption and/or electron transfer processes may alter the particle aggregation behavior and surface reactivity. In the present work, we have measured Ag^+ ions in AgNP aqueous suspension but in the absence of NZVI, to avoid sorption of released Ag^+ ions on iron oxide layer of NZVI surface. As a result, these dissolution tests were performed under oxidic (open atmosphere) or mild reducing conditions (anaerobic chamber), since the strong reducing conditions are ensured by the presence of NZVI. Under such conditions, Ag^+ can be detected, and released concentration was increased with increasing AgNP dose (See Fig. S10). However, examination of the thermodynamic database by means of Eh-pH diagrams of Ag species suggests that ions released through metal corrosion should be very limited, or even excluded, under the experimental conditions of this study (pH 9, -800 mV) (Brookins, 1988). Indeed, no ions can be detected at alkaline pH values and strongly reducing conditions, thereby ruling out galvanic effects between Ag^+ ions and inner Fe^0 within iron oxide shell. In addition, the same two-step behavior in NP removal kinetics by

NZVI was observed when AgNP has been replaced by TiO₂ (Fig. S3), further confirming the minor role of ions release and/or galvanic effect in the investigated systems.

Collectively, these results suggest that heteroaggregation of NZVI-AgNPs which is favorable at lower AgNP dose owing to the relatively lower energy barrier may alter the NZVI reactivity. As the AgNP dose increased, AgNP homoaggregation can be expected, thereby preventing potential alteration of the initial NZVI reactivity.

3.3. Spectroscopic investigations

To investigate the oxidation states of Ag and Fe in AgNP and NZVI suspensions, the XPS spectra of the Ag(3d) and Fe(2p) bands of AgNP, NZVI, and NZVI-AgNP suspensions were analyzed (Fig. 4). For AgNPs and NZVI-AgNPs, the Ag(3d_{5/2}) and Ag(3d_{3/2}) peaks at 368.6 and 374.6 eV were assigned to Ag(0) (Fig. 4(a)) (Xu et al., 2011), and the splitting of the 3d doublet of Ag (6.0 eV) confirmed the presence of Ag(0) (Chastain and King Jr, 1992; Xu et al., 2011).

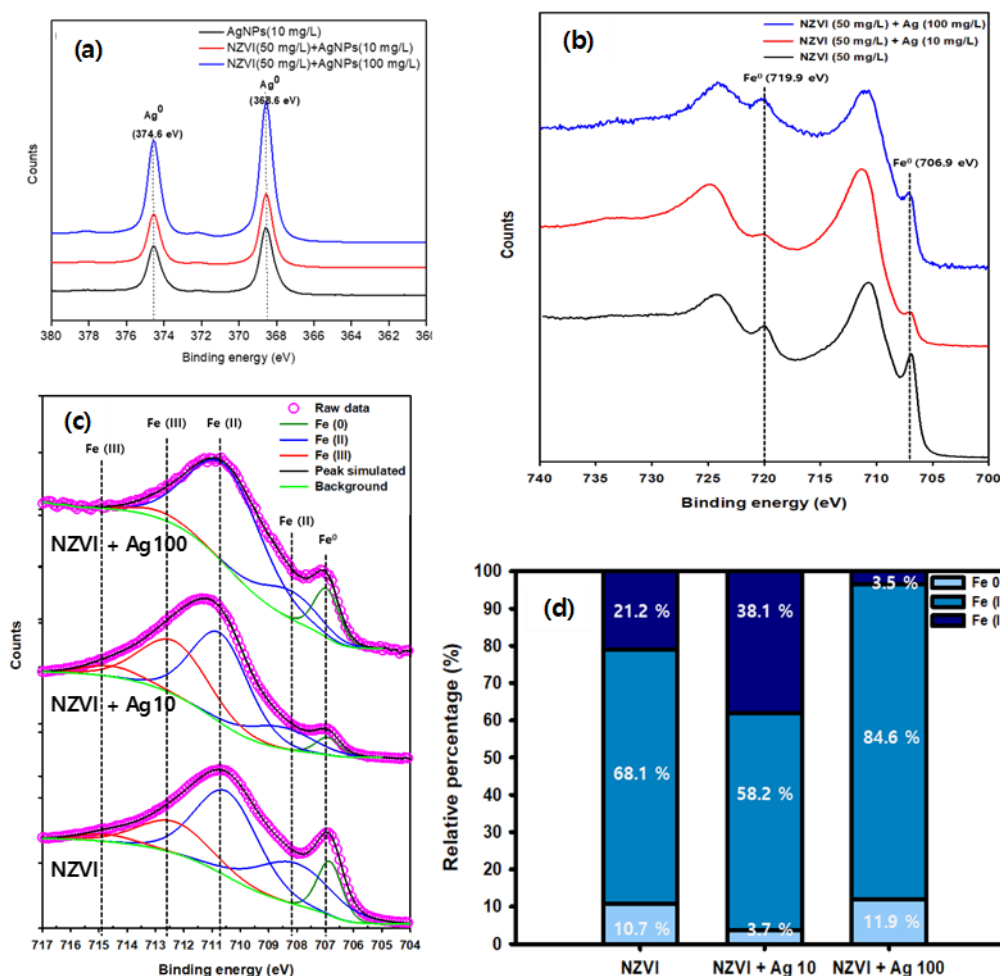


Figure 4. XPS spectra of (a) Ag(3d) in AgNP and NZVI-AgNP suspensions, (b) Fe(2p) in NZVI and NZVI-AgNP suspensions, (c) the corresponding deconvolution results of Fe(2p_{3/2}) (705–717 eV), and (d) relative percentage of iron species.

In the pristine NZVI, two distinct peaks were observed at 719.9 and 706.9 eV, which corresponded to the Fe(2p_{1/2}) and Fe(2p_{3/2}) of Fe(0) (Luo et al., 2014), respectively (Fig. 4(b)). In the NZVI-AgNP suspension, Fe(0) peaks were enhanced, indicating the presence of more Fe(0) on the NZVI surface after AgNPs were introduced (Li et al., 2009). The XPS spectra of Fe(2p_{3/2}) (Fig. 4(c)) showed five peaks at 706.9,

362 708.2–708.5, 710.3–710.7, 711.5–711.6, and 713.1–713.7 eV, which were assigned to
363 the binding energies of Fe(0) (706.5–707.0 eV), Fe(II)–O (708.2–710.9 eV), and
364 Fe(III)–O (711.0–714.0 eV). The proportion of Fe(0) (10.7%) and Fe(II) (68.1%) on
365 the NZVI surfaces significantly decreased to 3.7% and 58.2% after adding 10 mg/L
366 AgNPs, respectively (Fig. 4(d)). In contrast, their percentages dramatically increased
367 to 11.9% and 84.6% in the sample of NZVI with 100 mg/L AgNPs. These results
368 demonstrate that the presence of AgNPs decreased and increased the Fe(0) content on
369 the NZVI surface, which are in agreement with the results of degradation kinetics in
370 Fig. 2(b). This is also consistent with the TEM–EDS results (Fig. S8(c)), which showed
371 a thinner oxide layer on the NZVI surface at a higher AgNP dose. Previous
372 investigations have shown that the collision and friction between particles might occur
373 in suspensions under stirring conditions (Xie and Luo, 2018). In addition, these particle-
374 particle interactions become much stronger when both particle size and solid loading
375 increased (Xie and Luo, 2018). In our systems, higher AgNP doses enabled
376 homoaggregation and an increase in aggregate size (Fig. S11), likely inducing more
377 collision between large-sized AgNP aggregates and NZVI. This phenomenon likely
378 contributed to the peeling of the NZVI surface layer, which further resulted in the
379 exposure of the NZVI inner core. These results suggest that a higher AgNP dose led to
380 the partial removal of the iron oxide shell of NZVI through collisions between AgNP
381 homoaggregates and NZVI. Self-assembled AgNPs with bigger sizes accelerated the
382 peeling of the Fe oxide shell on the NZVI surface, thereby increasing the exposure of

inner Fe(0), and consequently, enhancing the *p*-NP removal. This also explains the enhanced NZVI reactivity under an increasing dose of sand microparticles (Fig. S5). As sand microparticles are inert and have a low surface area (0.06 m²/g), the enhanced NZVI reductive ability may be attributed to collision-driven processes in an aqueous suspension.

3.4. Effects of groundwater constituents on nanoparticles interaction and reactivity

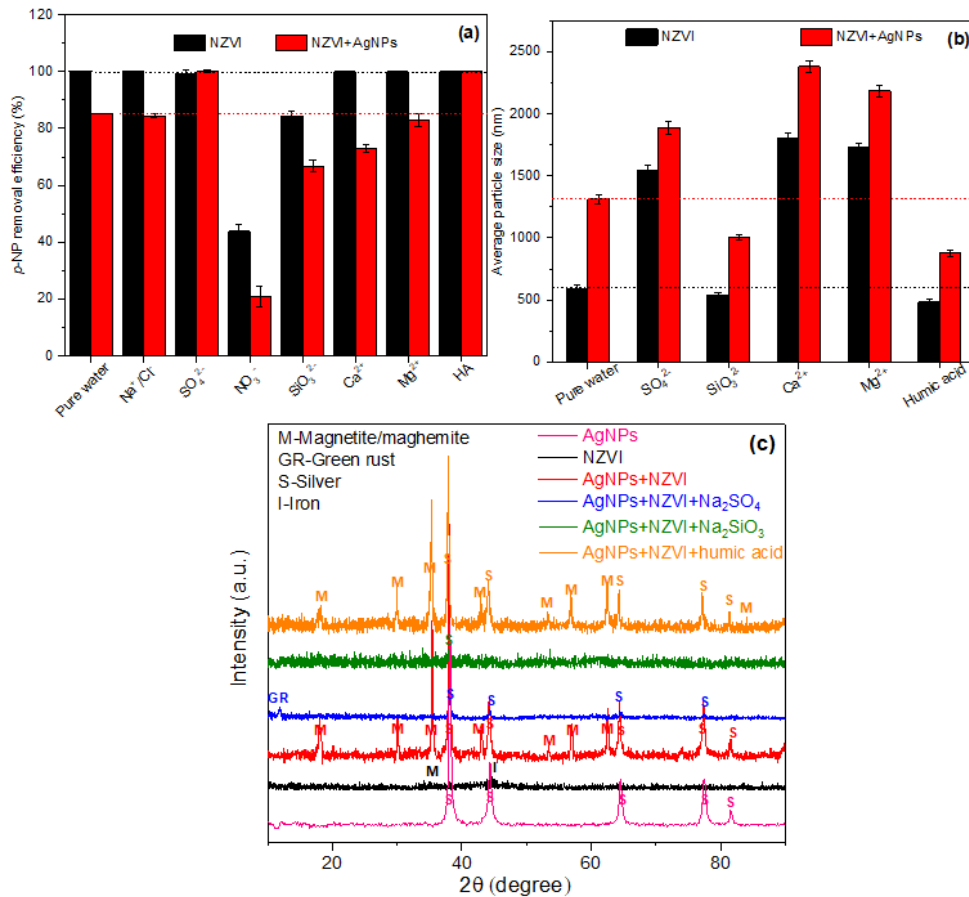


Figure 5. (a) Removal efficiencies of *p*-NP (2 h reaction) by NZVI and NZVI+AgNPs in the presence of co-existing groundwater solutes; (b) Average particle size of NZVI

and AgNP–NZVI complexes in the presence of non-competing groundwater solutes; (c) XRD pattern of the resulting products after the reaction of *p*-NP with non-competing groundwater solutes. Experimental conditions: [*p*-NP]_{initial} = 0.1 mM; [NZVI] = 50 mg/L; [AgNPs] = 10 mg/L; pH = 9.0±0.2; [Na⁺/Cl⁻] = 5 mM; [SO₄²⁻] = 1 mM; [NO₃⁻] = 0.5 mM; [SiO₃²⁻] = 0.5 mM; [Ca²⁺] = 2 mM; [Mg²⁺] = 2 mM; and [HA] = 5 mg/L.

In the environment, the concentration of AgNPs is normally much lower than those of NZVI used for remediation purposes (Su et al., 2013; McGillicuddy et al., 2018), the inhibition effect of AgNPs to NZVI would be more significant in natural systems. To evaluate the inhibition effects of AgNPs on the NZVI reactivity in conditions that emulate natural systems, the *p*-NP reduction in NZVI (50 mg/L) and AgNP (10 mg/L) suspensions was investigated in the presence of naturally occurring cations, anions, and organic matter. Experiments were conducted with groundwater constituents and humic acids (HAs) at levels similar to those encountered in real groundwater (Fig. 5(a)) (Edmunds and Shand, 2008). No impact of NaCl was observed. In the presence of most groundwater solutes, NZVI exhibited good performance for *p*-NP removal, with 100% removal over 2 h, except in the presence of NO₃⁻ (44%) and SiO₃²⁻ (84%). For NO₃⁻, the inhibitive result could be caused by a competitive reduction of NO₃⁻ by NZVI (Ryu et al., 2011). Compared to NZVI-AgNPs in pure water (85%), the removal efficiency of *p*-NP by the NZVI-AgNPs with NO₃⁻, SiO₃²⁻, Ca²⁺, and Mg²⁺ decreased to 21%, 67%, 73%, and 83%, respectively. Furthermore, *p*-NP was completely removed over 2 h in

the presence of SO_4^{2-} and HA, which represents a better performance than that obtained in pure water.

To further clarify the aggregation behavior of the particles, we measured the average particle sizes of NZVI and AgNP–NZVI suspensions in the presence of SO_4^{2-} , SiO_3^{2-} , Ca^{2+} , Mg^{2+} , and HA (Fig. 5(b)). As expected, the particles sizes in the NZVI–AgNP systems were higher than in systems without AgNPs, which was attributed to the heteroaggregation between AgNPs and NZVI particles. Upon the introduction of Ca^{2+} or Mg^{2+} , the particle size drastically increased from 593 nm to 1804 and 1727 nm in the NZVI system, and from 1313 nm to 2382 and 2186 nm in the NZVI–AgNP system, respectively. This was attributed to the particle surface charge screening (EDL contraction) by $\text{Ca}^{2+}/\text{Mg}^{2+}$ (Rogozhnikov, 2001). EDL contraction can decrease the electrostatic or steric repulsive forces of the nanoparticles, thereby increasing aggregation (Petosa et al., 2010) and further decreasing the NZVI reactivity (Ryu et al., 2011). Moreover, Ca^{2+} and Mg^{2+} showed stronger inhibitive effects in NZVI–AgNPs than in NZVI alone. In the presence of Ca^{2+} or Mg^{2+} , electrostatic repulsive forces among particles (i.e., NZVI–NZVI, NZVI–AgNP, AgNP–AgNP) favored homoaggregation and heteroaggregation, thus altering the NZVI reactivity.

In contrast, a decrease in the average particle size of NZVI (from 593 to 486 nm) and NZVI–AgNPs (from 1313 to 877 nm) in the presence of HA was attributed to the interactions of HA with the surfaces, which likely enhanced the electrostatic repulsion decreased (Dong and Lo, 2013). This reduced particle aggregation, which enhanced the

removal of *p*-NP. The particle size decreased more for NZVI-AgNPs than for NZVI, which suggests that less AgNPs were attached to NZVI surfaces, thereby providing a lower inhibition effect of AgNPs in the presence of HA.

XRD analysis was also conducted to analyze the passivation byproducts of NZVI-AgNPs after the reaction (Fig. 5(c)). The byproducts in the pure water system included maghemite (γ -Fe₂O₃)/magnetite (Fe₃O₄) and silver (Ag(0)), which were attributed to NZVI oxidation during the *p*-NP reduction (Xiong et al., 2018). Similarly, in the presence of HA, maghemite/magnetite and silver (Ag(0)) phases were also detected after *p*-NP removal. In contrast, green rust ($[\text{Fe}^{2+}_4\text{Fe}^{3+}_2(\text{HO}^-)_{12}]^{2+} \cdot [\text{SO}_4^{2-} \cdot 2\text{H}_2\text{O}]^{2-}$) (Tahawy et al., 2021) and silver (Ag(0)) were detected in the presence of SO₄²⁻. Considering the relatively higher reactivity of green rust than that of magnetite (Digiacoimo et al., 2020; Usman et al., 2018), the enhanced *p*-NP removal in the NZVI-AgNP-SO₄²⁻ system (Fig. 5(a)) was attributed to the generated green rust. For SiO₃²⁻, a weak peak of silver was identified as the final product, and there was no obvious Fe phase detected in the XRD analysis. The absence of Fe phases might be attributed to the amorphous coating of Si on the NZVI surface as previously reported, and the surface coated Si would further reduce the amount of active surface sites available for contaminants (Meng et al., 2002). Despite the lower particle size of NZVI-AgNP-SiO₃²⁻, the reactivity of both NZVI and NZVI-AgNPs decreased drastically, which was attributed to the strong binding of silicates to the NZVI surface.

4. Conclusions

Because of the increasing use of engineered nanoparticles (ENPs) in various industries and consumer items, ENPs are ubiquitously found in aquatic environments. However, little is known about the interactions among the co-existing ENPs in nature. This work showed for the first time how two typical engineered nanoparticles, nanoscale zero-valent iron (NZVI) and silver nanoparticles (AgNPs), interact and influence each other under environmentally-relevant conditions. First, we have investigated the potential interactions between AgNPs and NZVI particles using *p*-NP conversion into *p*-AP as a probe reaction. At a AgNP load of 10 mg/L, AgNPs covered the reactive NZVI surfaces, which decreased *p*-NP removal. Whereas at a AgNP load of 100 mg/L, the enhanced homoaggregation of AgNPs led to the exposure of the inner Fe(0) surface of NZVI because of particle collisions, which increased the *p*-NP removal. The same behavior was observed with nanosized TiO₂ particles and micro-sized quartz sand particles, thereby excluding the role of potential Ag⁺ ions release, electron transfer process, and/or galvanic effect.

Second, the impact of groundwater constituents has been evaluated, which showed contrasting effects depending on ion types and the binding affinities to Fe-oxides. These results revealed that not only AgNPs but also other nano/micro-sized particles (e.g. TiO₂ and quartz sand) may influence the NZVI reactivity, which will help to develop decision support and prediction tools for NZVI remediation technologies. Electron microscopic and X-ray spectroscopic investigations and DLVO calculations revealed that heteroaggregation of NZVI and AgNPs resulted in dramatic decrease of the NZVI

477 reactivity, while at higher AgNPs loading, collision between self-assembled aggregates
478 of AgNPs and NZVI can improve the reductive ability of NZVI. These findings shed
479 light on an overlooked aspect of interactions between co-existing nanoparticles, which
480 could influence their fate and mobility in environmental settings. Owing to the
481 increasing occurrence of NPs in aqueous environments, this work calls for more
482 investigations of potential interactions between the co-occurring nanomaterials for
483 accurate assessment of environmental associated risks.

484 **Conflicts of interest**

485 There are no conflicts to declare.

486 **Acknowledgments**

487 We would like to acknowledge the support from Korea Environment Industry &
488 Technology Institute (KEITI) through “Subsurface Environmental Management (SEM)
489 Project”, funded by Korea Ministry of Environment (MOE) (2020002480006). We are
490 also grateful for the assistance of Isabelle Soutrel (LC/UV) and Vincent Dorcet
491 (THEMIS platform).

References

- Abbas, Q., Yousaf, B., Amina, Ali, M.U., Munir, M.A.M., El-Naggar, A., Rinklebe, J., Naushad, M., 2020. Transformation pathways and fate of engineered nanoparticles (ENPs) in distinct interactive environmental compartments: A review. *Environ. Int.* 138, 105646.
- Asghari, S., Johari, S.A., Ji, H.L., Yong, S.K., Yong, B.J., Choi, H.J., Min, C.M., Yu, I.J., 2012. Toxicity of various silver nanoparticles compared to silver ions in *Daphnia magna*. *J. Nanobiotechnology* 10(1), 1-11.
- Auffan, M., Pedetour, M., Rose, J., Masion, A., Ziarelli, F., Borschneck, D., Chaneac, C., Botta, C., Chaurand, P., Labille, J., Bottero, J.-Y., 2010. Structural Degradation at the Surface of a TiO₂-Based Nanomaterial Used in Cosmetics. *Environ. Sci. Technol.* 44(7), 2689-2694.
- Bae, S., Gim, S., Kim, H., Hanna, K., 2016. Effect of NaBH₄ on properties of nanoscale zero-valent iron and its catalytic activity for reduction of p-nitrophenol. *Appl. Catal., B* 182, 541-549.
- Bae, S., Hanna, K., 2015. Reactivity of nanoscale zero-valent iron in unbuffered systems: effect of pH and Fe (II) dissolution. *Environ. Sci. Technol.* 49(17), 10536-10543.
- Bae, S., Lee, W., 2014. Influence of Riboflavin on Nanoscale Zero-Valent Iron Reactivity during the Degradation of Carbon Tetrachloride. *Environ. Sci. Technol.* 48(4), 2368-2376.
- Brookins D.G. Eh- pH diagrams of geochemistry. Springer-Verlag, New York (1988).
- Chastain, J., King Jr, R.C., 1992. Handbook of X-ray photoelectron spectroscopy. Perkin-Elmer Corporation 40, 221.
- Danail, H., Ineke, M., 2009. Hazards and Risks of Engineered Nanoparticles for the Environment and Human Health. *Sustainability* 1(4), 1161-1161.
- Deng, H., McShan, D., Zhang, Y., Sinha, S.S., Arslan, Z., Ray, P.C., Yu, H., 2016. Mechanistic study of the synergistic antibacterial activity of combined silver nanoparticles and common antibiotics. *Environ. Sci. Technol.* 50(16), 8840-8848.
- Deng, J., Bae, S., Yoon, S., Pasturel, M., Marsac, R., Hanna, K., 2020. Adsorption capacity of the corrosion products of nanoscale zerovalent iron for emerging contaminants. *Environ. Sci. Nano* 7(12), 3773-3782.
- Digiaco, F., Tobler, D.J., Held, T., Neumann, T., 2020. Immobilization of Cr(VI) by sulphate green rust and sulphidized nanoscale zerovalent iron in sand media: batch and column studies. *Geochem. Trans.* 21(1), 8.

529 Dong, H., Lo, I.M.C., 2013. Influence of humic acid on the colloidal stability of surface-
530 modified nano zero-valent iron. *Water Res.* 47(1), 419-427.

531 Du, Y., Chen, H., Chen, R., Xu, N. 2004. Synthesis of p-aminophenol from p-
532 nitrophenol over nano-sized nickel catalysts. *Appl. Catal. A-Gen* 277(1), 259-264.

533 Echegoyen, Y., Nerín, C., 2013. Nanoparticle release from nano-silver antimicrobial
534 food containers. *Food Chem. Toxicol.* 62, 16-22.

535 Edmunds, W.M., Shand, P., 2008. Natural groundwater quality.

536 Hernández-Gordillo, A., Arroyo, M., Zanella, R., Rodríguez-González, V. 2014.
537 Photoconversion of 4-nitrophenol in the presence of hydrazine with AgNPs-TiO₂
538 nanoparticles prepared by the sol-gel method. *J. Hazard. Mater.* 268, 84-91.

539 Joo, S.H., Feitz, A.J., Waite, T.D., 2004. Oxidative Degradation of the Carbothioate
540 Herbicide, Molinate, Using Nanoscale Zero-Valent Iron. *Environ. Sci. Technol.* 38(7),
541 2242-2247.0.799

542 Lai, B., Zhang, Y.-H., Li, R., Zhou, Y.-X., Wang, J., 2014. Influence of operating
543 temperature on the reduction of high concentration p-nitrophenol (PNP) by zero valent
544 iron (ZVI). *Chem. Eng. J.* 249, 143-152.

545 Li, S., Wang, W., Liang, F., Zhang, W.-x., 2017. Heavy metal removal using nanoscale
546 zero-valent iron (nZVI): Theory and application. *J. Hazard. Mater.* 322, 163-171.

547 Li, S., Yan, W., Zhang, W.-x., 2009. Solvent-free production of nanoscale zero-valent
548 iron (nZVI) with precision milling. *Green Chem.* 11(10), 1618-1626.

549 Lin, S., Cheng, Y., Liu, J., Wiesner, M.R., 2012. Polymeric Coatings on Silver
550 Nanoparticles Hinder Autoaggregation but Enhance Attachment to Uncoated Surfaces.
551 *Langmuir* 28(9), 4178-4186.

552 Liu, Y., Lowry, G.V., 2006. Effect of Particle Age (Fe₀ Content) and Solution pH On
553 NZVI Reactivity: H₂ Evolution and TCE Dechlorination. *Environ. Sci. Technol.*
554 40(19), 6085-6090.

555 Lorenz, C., Windler, L., von Goetz, N., Lehmann, R.P., Schuppler, M., Hungerbühler,
556 K., Heuberger, M., Nowack, B., 2012. Characterization of silver release from
557 commercially available functional (nano)textiles. *Chemosphere* 89(7), 817-824.

558 Luo, S., Lu, T., Peng, L., Shao, J., Zeng, Q., Gu, J.-D., 2014. Synthesis of nanoscale
559 zero-valent iron immobilized in alginate microcapsules for removal of Pb(II) from
560 aqueous solution. *J. Mater. Chem. A* 2(37), 15463-15472.

561 Lützenkirchen, J., Preočanin, T. and Kallay, N. 2008. A macroscopic water structure
562 based model for describing charging phenomena at inert hydrophobic surfaces in
563 aqueous electrolyte solutions. *Phys. Chem. Chem. Phys.* 10(32), 4946-4955.

564 Mahdi, K.N.M., Peters, R.J.B., Klumpp, E., Bohme, S., Ploeg, M.v.d., Ritsema, C.,

565 Geissen, V., 2017. Silver nanoparticles in soil: Aqueous extraction combined with
 566 single-particle ICP-MS for detection and characterization. *Environ. Nanotechnol.*
 567 *Monit. Manag.* 7, 24-33.

568 McGillicuddy, E., Morrison, L., Cormican, M., Dockery, P., Morris, D., 2018. Activated
 569 charcoal as a capture material for silver nanoparticles in environmental water samples.
 570 *Sci. Total Environ.* 645, 356-362.

571 Meng, X., Korfiatis, G.P., Bang, S., Bang, K.W., 2002. Combined effects of anions on
 572 arsenic removal by iron hydroxides. *Toxicol. Lett.* 133(1), 103-111.

573 Mueller, N.C., Braun, J., Bruns, J., Černík, M., Rissing, P., Nowack, R.B., 2012.
 574 Application of nanoscale zero valent iron (NZVI) for groundwater remediation in
 575 Europe. *Environ. Sci. Pollut. Res.* 19(2), 550-558.

576 Petosa, A.R., Jaisi, D.P., Quevedo, I.R., Elimelech, M., Tufenkji, N., 2010. Aggregation
 577 and deposition of engineered nanomaterials in aquatic environments: role of
 578 physicochemical interactions. *Environ. Sci. Technol.* 44(17), 6532-6549.

579 Phenrat, T., Thongboot, T., Lowry, G.V., 2016. Electromagnetic Induction of Zerovalent
 580 Iron (ZVI) Powder and Nanoscale Zerovalent Iron (NZVI) Particles Enhances
 581 Dechlorination of Trichloroethylene in Contaminated Groundwater and Soil: Proof of
 582 Concept. *Environ. Sci. Technol.* 50(2), 872-880.

583 Poudel, M.B., Karki, H.P. and Kim, H.J. (2020) Silver nanoparticles decorated
 584 molybdenum sulfide/tungstate oxide nanorods as high performance supercapacitor
 585 electrode. *Journal of Energy Storage* 32, 101693.

586 Poudel, M.B. and Kim, H.J., 2022. Confinement of Zn-Mg-Al-layered double
 587 hydroxide and α -Fe₂O₃ nanorods on hollow porous carbon nanofibers: A free-standing
 588 electrode for solid-state symmetric supercapacitors. *Chem. Eng. J.* 429, 132345.

589 Poudel, M.B., Shin, M. and Joo Kim, H., 2022. Interface engineering of MIL-88 derived
 590 MnFe-LDH and MnFe₂O₃ on three-dimensional carbon nanofibers for the efficient
 591 adsorption of Cr(VI), Pb(II), and As(III) ions. *Sep. Purif. Technol.* 287, 120463.

592 Poudel, M.B., Shin, M. and Kim, H.J. (2021) Polyaniline-silver-manganese dioxide
 593 nanorod ternary composite for asymmetric supercapacitor with remarkable
 594 electrochemical performance. *International Journal of Hydrogen Energy* 46(1), 474-
 595 485.

596 Rogozhnikov, N.A., 2001. Effect of Alkali Metal Cations on the EDL Structure at a
 597 Gold Electrode in Alkali Solutions. *Russ. J. Electrochem.* 37(10), 1101-1107.

598 Ryu, A., Jeong, S.-W., Jang, A., Choi, H., 2011. Reduction of highly concentrated
 599 nitrate using nanoscale zero-valent iron: Effects of aggregation and catalyst on
 600 reactivity. *Appl. Catal., B* 105(1-2), 128-135.

601 Shen, W., Zhang, X., Huang, Q., Xu, Q., Song, W., 2014. Preparation of solid silver

nanoparticles for inkjet printed flexible electronics with high conductivity. *Nanoscale* 6(3), 1622-1628.

Sohn, K., Kang, S.W., Ahn, S., Woo, M., Yang, S.-K., 2006. Fe (0) nanoparticles for nitrate reduction: stability, reactivity, and transformation. *Environ. Sci. Technol.* 40(17), 5514-5519.

Sridhar, R., Lakshminarayanan, R., Madhaiyan, K., Barathi, V.A., Lim, K.H.C., Ramakrishna, S., 2015. Electrospayed nanoparticles and electrospun nanofibers based on natural materials: applications in tissue regeneration, drug delivery and pharmaceuticals. *Chem. Soc. Rev.* 44(3), 790-814.

Stefaniuk, M., Oleszczuk, P., Ok, Y.S., 2016. Review on nano zerovalent iron (nZVI): From synthesis to environmental applications. *Chem. Eng. J.* 287, 618-632.

Su, C., Puls, R.W., Krug, T.A., Watling, M.T., O'Hara, S.K., Quinn, J.W., Ruiz, N.E. 2013. Travel distance and transformation of injected emulsified zerovalent iron nanoparticles in the subsurface during two and half years. *Water Research* 47(12), 4095-4106.

Syafiuddin, A., Salmiati, S., Hadibarata, T., Kueh, A.B.H., Salim, M.R., Zaini, M.A.A., 2018. Silver Nanoparticles in the Water Environment in Malaysia: Inspection, characterization, removal, modeling, and future perspective. *Sci. Rep.* 8(1), 1-15.

Tahawy, R., Doustkhah, E., Abdel-Aal, E.-S.A., Esmat, M., Farghaly, F.E., El-Hosainy, H., Tsunoji, N., El-Hosiny, F.I., Yamauchi, Y., Assadi, M.H.N., Ide, Y., 2021. Exceptionally stable green rust, a mixed-valent iron-layered double hydroxide, as an efficient solar photocatalyst for H₂ production from ammonia borane. *Appl. Catal., B* 286, 119854.

Tsarev, S., Collins, R.N., Ilton, E.S., Fahy, A., Waite, T.D., 2017. The short-term reduction of uranium by nanoscale zero-valent iron (nZVI): role of oxide shell, reduction mechanism and the formation of U(v)-carbonate phases. *Environ. Sci. Nano* 4(6), 1304-1313.

Usman, M., Byrne, J.M., Chaudhary, A., Orsetti, S., Hanna, K., Ruby, C., Kappler, A., Haderlein, S.B., 2018. Magnetite and Green Rust: Synthesis, Properties, and Environmental Applications of Mixed-Valent Iron Minerals. *Chem. Rev.* 118(7), 3251-3304.

Vilardi, G. 2019. Mathematical modelling of simultaneous nitrate and dissolved oxygen reduction by Cu-nZVI using a bi-component shrinking core model. *Powder Technol.* 343, 613-618.

Vilardi, G., Parisi, M., Verdone, N. 2019. Simultaneous aggregation and oxidation of nZVI in Rushton equipped agitated vessel: Experimental and modelling. *Powder Technol.* 353, 238-246.

639 Vilardi, G. 2020. P-aminophenol catalysed production on supported nano-magnetite
640 particles in fixed-bed reactor: Kinetic modelling and scale-up. *Chemosphere* 250,
641 126237.

642 Wang, R., Dang, F., Liu, C., Wang, D.-j., Cui, P.-x., Yan, H.-j., Zhou, D.-m., 2019.
643 Heteroaggregation and dissolution of silver nanoparticles by iron oxide colloids under
644 environmentally relevant conditions.. *Environ. Sci. Nano.* 6(1), 195-206.

645 Wei, Y.-T., Wu, S.-C., Chou, C.-M., Che, C.-H., Tsai, S.-M., Lien, H.-L., 2010.
646 Influence of nanoscale zero-valent iron on geochemical properties of groundwater and
647 vinyl chloride degradation: A field case study. *Water Res.* 44(1), 131-140.

648 Xia, X., Ling, L., Zhang, W.-x., 2017. Genesis of pure Se(0) nano- and micro-structures
649 in wastewater with nanoscale zero-valent iron (nZVI). . *Environ. Sci. Nano* 4(1), 52-59.

650 Xie, L., Luo, Z.-H., 2018. Modeling and simulation of the influences of particle-particle
651 interactions on dense solid–liquid suspensions in stirred vessels. *Chem. Eng. Sci.* 176,
652 439-453.

653 Xiong, Z., Lai, B., Yang, P., 2018. Enhancing the efficiency of zero valent iron by
654 electrolysis: Performance and reaction mechanism. *Chemosphere* 194, 189-199.

655 Xu, F., Pieltt, C., Farkas, S., Qazzaz, M., Syed, N.I., 2013. Silver nanoparticles (AgNPs)
656 cause degeneration of cytoskeleton and disrupt synaptic machinery of cultured cortical
657 neurons. *Mol. Brain* 6(1), 29-29.

658 Xu, H., Shi, X., Ma, H., Lv, Y., Zhang, L., Mao, Z., 2011. The preparation and
659 antibacterial effects of dopa-cotton/AgNPs. *Appl. Surf. Sci.* 257(15), 6799-6803.

660 Yu, S.J., Yin, Y.G., Chao, J.B., Shen, M.H., Liu, J.F., 2014. Highly dynamic PVP-coated
661 silver nanoparticles in aquatic environments: chemical and morphology change induced
662 by oxidation of Ag(0) and reduction of Ag(+). *Environ. Sci. Technol.* 48(1), 403-411.

663 Zhu, X., Zhou, L., Li, Y., Han, B., Feng, Q., 2021. Rapid Degradation of Carbon
664 Tetrachloride by Microscale Ag/Fe Bimetallic Particles. *Int. J. Env. Res. Public Health*
665 18(4), 2124.

666 Zhuang, Y., Ahn, S., Seyfferth, A.L., Masue-Slowey, Y., Fendorf, S., Luthy, R.G., 2011.
667 Dehalogenation of polybrominated diphenyl ethers and polychlorinated biphenyl by
668 bimetallic, impregnated, and nanoscale zerovalent iron. *Environ. Sci. Technol.* 45(11),
669 4896-4903.

670